

*Research Article*

# Expandable Orbit Decay Prediction Using Continual Learning

**Junhua He**  <sup>1,2</sup> **Hua Wang**  <sup>1,2</sup> **Haitao Wang**  <sup>1,2</sup> **Xuankun Fang**  <sup>1,2</sup>  
**and Chengyi Huo**  <sup>1,2</sup>

<sup>1</sup>College of Aerospace Science and Engineering, National University of Defense Technology, Changsha 410073, China

<sup>2</sup>Hunan Key Laboratory of Intelligent Planning and Simulation for Aerospace Missions, Changsha 410073, China

Correspondence should be addressed to Hua Wang; wanghua@nudt.edu.cn

Received 31 May 2024; Accepted 19 July 2024

Academic Editor: Christian Circi

Copyright © 2024 Junhua He et al. This is an open access article distributed under the Creative Commons Attribution License, which permits unrestricted use, distribution, and reproduction in any medium, provided the original work is properly cited.

Very low earth orbit (VLEO) spacecraft have become an attractive proposition with obvious advantages in various missions, including communication and ground observation. Higher requirements for precise orbit decay prediction (PODP) technology are requested, which provides accurate state references for orbit maintenance and necessary database for space situational awareness. The effectiveness of the traditional orbital prediction method for PODP is limited by inaccurate estimation of the spacecraft's physical parameters and space environments. Generalization performance of machine learning techniques (MLTs) is blocked by the universal challenge known as catastrophic forgetting, resulting in limited improvement on PODP. In this study, a method of expandable orbit decay propagator (EODP) for spacecraft PODP in VLEO, based on model-agnostic MLTs, is proposed. The plasticity of the proposed model is discussed, which originates from the uncertainty of neural network (NN) parameters. The proposed method overcomes the negative effects of uncertain physical parameters and complex space environments. The model achieves at least a 70% improvement in accuracy compared to the high-precision orbital propagator (HPOP) and presents a novel approach for the future implementation of machine learning-based methods in the field of orbit prediction.

## 1. Introduction

Very low earth orbit (VLEO) is an orbit with a nominal altitude of about 450 km or less, which is much lower than the conventional low earth orbit (LEO) with an altitude of 600–1200 km and the geostationary earth orbit (GEO) with an altitude of 35,768 km [1]. Compared to higher orbits, VLEO spacecraft have lower launch costs, better radiometric performance, and better resolution of optical payloads [2]. With the effect of dense atmosphere, space debris in VLEO experiences a more rapid decay rate. Compared to higher altitudes, spacecraft in VLEO are subject to less impact from space debris.

VLEO spacecraft possess unique advantages in ground observation, emergency communication, and geophysical scientific exploration, attracting interest from both national and commercial entities [3]. To facilitate material supply

and reduce the threat of space debris, both the International Space Station and Chinese Space Station are located at orbital altitudes below 450 km [4, 5]. ESA's first Core Earth Explorer mission, GOCE, is aimed at measuring the precise gravity gradient at an altitude of 250 km [6]. The US Naval Research Laboratory has launched two spherical satellites, ANDE Pollux and ANDE Castor, to improve the accuracy of LEO spacecraft orbit prediction by detecting the overall atmospheric density at an altitude of 400 km [7]. JAXA launched the Super Low Altitude Orbit Test Satellite in 2017 to test high-resolution satellite images within an altitude range of 160–270 km [8]. Commercial aerospace companies operating giant constellations, such as Starlink, also consider VLEO as the next expansion direction.

Despite the advantages of VLEO spacecraft, the challenges they encounter are evident: Atmospheric drag will significantly shorten their lifetime [9]. Large-scale spacecraft,

such as the Space Station, require frequent orbital altitude boosts to meet mission requirements. Fuel for the space station can be replenished regularly, while other spacecraft often use high specific impulse propulsion technology to extend their service time. When fuel equals life, precise orbit decay prediction (PODP) becomes an important prerequisite for long-term on-orbit service. PODP provides a reliable reference for maneuvering strategies for orbit maintenance, proving to be an effective method for enhancing fuel efficiency.

PODP faces a series of challenges in practical situations. The traditional orbital prediction methods (TOPMs) based on physical models are inaccurate with divergent errors in PODP due to the challenges of modeling the atmosphere and acquiring the physical information of specific spacecraft [10]. Orbit decay with TOPM also depends on the information of space environment, which is hard to accurately predict. In recent years, several methods with machine learning techniques (MLTs) have emerged to enhance the capabilities of TOPM. Cimmino, Oppomolla, and Fasano [11] used MLT to determine the ballistic coefficients of LEO spacecraft based on orbital data. This approach can minimize prediction errors stemming from uncertainties in drag coefficients and area-to-mass ratios. Lei and Zhang [12] employed another form of proximal policy optimization, PPO2, to adjust atmosphere model parameters to improve TOPM. Compared to standard orbital data, the proposed method resulted in a maximum absolute space position error of 8133.329 m on the CSS in 3 days. Peng and Bai [13] used an artificial neural network (NN) to compensate for TOPM errors. Compared to the high-precision orbital propagator (HPOP), the proposed approach significantly reduced residual errors. Li et al. [14] captured the error patterns to adjust the physical model with MLT based on historical prediction errors of space debris, which enhanced the capability of space situational awareness. Bizalion et al. [15] used MLT to derive the underlying patterns of historical error from two-line element (TLE) data, which was successful in generating valuable covariance information for a significant portion of the TLE directory.

In addition to indirectly improving TOPM with MLT, only a limited number of studies have concerned model-agnostic orbit prediction technology. Thammawichai and Luangwilai [16] proposed the nonlinear programming model to generate orbital elements based on publicly available TLE data. Relative to the SGP4 model, the proposed approach performed better. Luo, Ren, and Zhao [17] used an LSTM-CNN model and trained it with TLE data of LEO spacecraft, which resulted in an overall position error of about 200 km after 20 days.

Excluding considerations of physical models, the utilization of PODP in combination with model-agnostic MLT offers enhanced flexibility and requires lower computational resources and memory usage compared to TOPM. Furthermore, it mitigates the inherent structural bias associated with physical models and is well suited for scenarios characterized by abundant data availability. The dynamic factors influencing the decay, such as the space environment and spacecraft physical parameters, pose a challenge of

catastrophic forgetting [18] for conventional MLT. Current model-agnostic MLTs face limitations in terms of their generalization capabilities. Various strategies have been extensively explored to enhance the generalization performance of NNs [19], including optimization-based methods (like meta-learning [20]), replay-based techniques (such as experience replay [21]), and regularization-based approaches (like elastic weight consolidation [EWC] [22]). Meta-learning seeks to achieve “learning to learn,” allowing NN to be flexible and adaptable in various scenarios, which has been utilized in the field of spacecraft terminal autonomous navigation and control [23–25]. Experience replay involves the creation of a small memory buffer to retain samples from previous tasks, allowing the NN to retain learned skills. This technique has been explored in spacecraft collision avoidance [26] and integrated scheduling [27]. The EWC combines historical and recent training data to update the NN parameters by applying a penalty function, commonly used to process large datasets by decomposing them into several subsets in the field of earth observation [28]. Meta-learning methods excel in few-shot learning, and experience replay efficiently constructs and utilizes memory buffers with a limited sample size. EWC is particularly suited for regression problems with abundant training data.

In this paper, the expandable orbit decay propagator (EODP) is proposed to achieve PODP of VLEO spacecraft based on model-agnostic MLT. EODP employs a deep NN (DNN) as the fundamental learner to comprehend the decaying rule and incorporates the theory of EWC. Compared to the previous method, EODP greatly improves prediction accuracy and generalization performance. Furthermore, it presents a novel approach for the future implementation of machine learning-based methods in the field of orbit prediction.

The remainder of the paper is organized as follows. First, a definition of training and testing set and an overview of the proposed EODP are provided. The plasticity of EODP is then analyzed, and the effects on the training process with different training methods are discussed. Compared to orbital data in real situations, the performance of EODP is analyzed. The results show that EODP achieves high accuracy in PODP of VLEO spacecraft and maintains excellent generalization when dealing with different spacecraft.

## 2. Methods

**2.1. Generation of Orbital Decay Training Set.** HPOP was adapted to generate the training set of VLEO spacecraft, and the effects of perturbations considered are shown in Table 1.

With the influence of the factors above, the state of spacecraft can be expressed as

$$\ddot{\mathbf{r}} = -\frac{\mu}{r^2} \left( \frac{\mathbf{r}}{r} \right) + \mathbf{a}_E + \mathbf{a}_D + \mathbf{a}_R + \mathbf{a}_{tr} \quad (1)$$

where  $\ddot{\mathbf{r}}$  and  $\mathbf{r}$  are the vectors of acceleration and position in the J2000 coordinate system,  $\mu$  is the earth gravitational constant,  $r$  is the geocentric distance, and  $\mathbf{a}_E$ ,  $\mathbf{a}_D$ ,  $\mathbf{a}_R$ ,  $\mathbf{a}_{tr}$  are the perturbation accelerations caused by the nonspherical earth

TABLE 1: Perturbation factors considered in the HPOP model.

Perturbation	Model	Detail
Nonspherical earth gravity	EGM2008 gravity model	$20 \times 20$ harmonics
Atmospheric drag	NRLMSISE 2000 atmospheric model	—
Solar radiation pressure	Spherical solar radiation pressure model	—
Three-body attraction	“Sun, moon, and earth” gravity model	—

gravity, atmospheric drag, solar radiation pressure, and three-body attraction, respectively.

Decaying rules of VLEO spacecraft are difficult to capture directly with osculating orbital elements, while using mean orbital elements is appropriate [29].

$$H(t) = h_{t_0} + a_{s1}(t - t_0) + a_{l2}(t - t_0) + a_{s2}(t - t_0) \dots \quad (2)$$

$$h_{t_0} = \bar{a}(t_0) - R \quad (3)$$

where  $H(t)$  is the orbital altitude at time instant  $t$ ;  $h_{t_0}$  is the initial altitude;  $\bar{a}(t_0)$  indicates initial mean orbit semimajor axis;  $R$  is the average equatorial radius of the earth; and  $a_{s1}$ ,  $a_{l2}$ , and  $a_{s2}$  are the first-order short-period factor, second-order long-period factor, and second-order short-period factor of the semimajor axis, respectively. Caused by the nonspherical earth gravity, the periodic terms of semimajor axis are associated with inclination [30], which can be described as

$$a_{s1}(t) = \frac{A_2}{a} \left\{ \frac{2}{3} \left( 1 - \frac{3}{2} \sin^2 i \right) \left[ \left( \frac{a}{r} \right)^3 - (1 - e^2)^{-3/2} \right] + \sin^2 i \left( \frac{a}{r} \right)^3 \cos 2(f + \omega) \right\} \cos^{-1} \theta \quad (4)$$

$$a_{l2}(t) = \left( \frac{a A_2^2}{p^4} \cos 2\omega \right) \left[ \left( \frac{7}{12} - \frac{19}{8} \sin^2 i \right) e^2 - \frac{1}{6} (4 - 5 \sin^2 i) \cos 2f \right] + \left( \frac{a A_2^2}{p^4} \frac{e^4}{1 - e^2} \right) \left[ \frac{7}{3} \left( 1 - \frac{3}{2} \sin^2 i \right) \cos 2\omega + \frac{1}{32} \sin^2 i \cos 4\omega \right] \quad (5)$$

$$A_2 = \frac{3}{2} J_2, p = a(1 - e^2) \quad (6)$$

where  $J_2$  is the EGM2008 zonal spherical harmonic coefficient of the gravitational potential to Degree 2. The  $a$ ,  $i$ ,  $f$ ,  $e$ , and  $\omega$  are the osculating orbital elements of semimajor axis, inclination, true anomaly, eccentricity, and argument of periapsis, respectively.

Nonspherical perturbation of the earth results in periodic alterations of  $a$ ,  $i$ , and  $e$ . The primary factor contributing to decay is atmospheric drag, which does not affect  $i$  [31], as shown in Figure 1. Inclinations exhibit notable variations across different spacecraft, thereby influencing the decay rule distinctly. For deriving decay rule at various  $i$ , the generation of the training data should account for the variability of  $i$ .

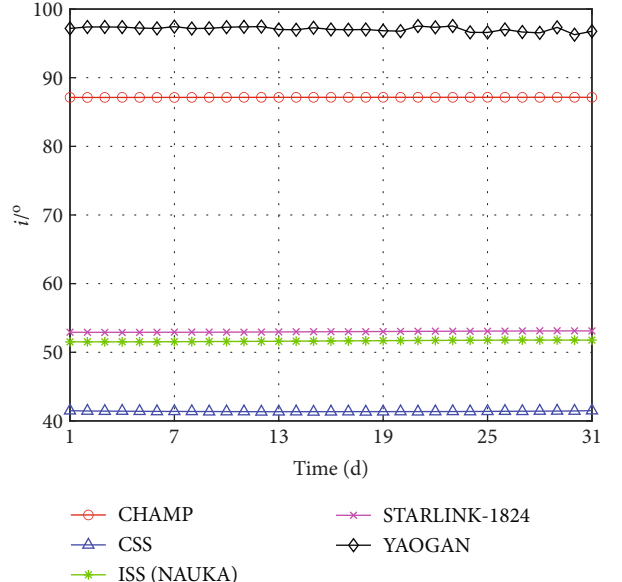


FIGURE 1: Daily variation in  $i$  of multiple VLEO spacecraft. Employing two-line element (TLE) sets and the SGP4 to determine the orbital parameters.

The calculation error of atmospheric drag is the main issue that affects the accuracy of TOPM [32]. The atmospheric drag acceleration can be expressed as

$$\mathbf{a}_D = -\frac{1}{2} C_d \left( \frac{S}{M} \right) \rho v^2 \hat{\mathbf{v}} \quad (7)$$

where  $\mathbf{a}_D$  is the acceleration caused by atmospheric drag,  $C_d$  is the drag coefficients,  $S$  and  $M$  are the effective resistance area and mass, respectively,  $\rho$  stands for atmospheric density at the current position,  $v$  is the velocity relative to airflow, and  $\hat{\mathbf{v}}$  is the unit vector of  $v$ .

Spacecraft usually lose the ability of attitude control during decay, which directly affects the effective drag area. Due to the complexity and variability of the atmosphere environment and attitude of the spacecraft, factors such as the angle of airflow, material properties of spacecraft surfaces, and atmospheric humidity will affect  $C_d$ . Accurate values of  $C_d$  and  $S/M$  are difficult to figure out when considering the above factors. To avoid the negative effect caused by determination errors of  $C_d$  and  $S/M$ , the generation of the training set should consider the variation of them.

Accurate modeling methods for the atmosphere have always been a concern. A series of achievements have been proposed, including the Harris–Priester model, which considers

weekly variations. Additionally, the three-dimensional atmospheric models DTM2012 and NRLMSIS 2000 take altitude, season, latitude, and weekly variations into account. Bowman et al. [33] introduced new exospheric temperature equations, semiannual density equations, and geomagnetic storm equations, which significantly reduce the density errors during major geomagnetic storm periods. The accuracy of atmospheric models is limited by the information of space weather, especially solar activity ( $F10.7$ ) and geomagnetism ( $K_p$ ) [34]. Characterizing atmospheric density with these two factors is reasonable and practicable. To avoid the negative effect caused by determination errors of atmospheric density, the generation of the training set should also consider the variations of  $F10.7$  and  $K_p$ .

In summary, the training set contains compositional information of six dimensions, and one sample can be represented as follows:

$$\text{Sample}_n = \langle K_p, F10.7, H, i, C_d, S/M \rangle \quad (8)$$

McCreary [35] put forward a series of recommendations for missions in VLEO, proposing the establishment of a circular sun-synchronous orbit with a semimajor axis of  $6608 \pm 70$  km. With reference to their suggestions, this study focuses on the VLEO spacecraft with circular or nearly circular orbits. The parameters of  $H$  and  $i$  are defined within the intervals of [150 km, 300 km] and [90°, 110°], respectively.

Observation data of  $F10.7$  from 1990-01-01 to 2014-12-31 is shown in Figure 2. The data is sourced from the Celestrak website.  $F10.7$  usually falls within the range of [65, 300]. In this study,  $F10.7$  is set within the range of 70–280 due to the low likelihood of extreme values.

The  $K_p$  typically uses 28 values to qualify the strength of geomagnetic activity [36], which can be described as

$$K_p = \frac{n_1}{3} \quad (n = 0, 1, 2 \dots, 27) \quad (9)$$

For  $C_d$  and  $S/M$ , there are no standardized criteria, which can be set as follows:

$$\begin{cases} S/M = [0.005, 0.01, 0.015, 0.02] \text{ (m}^2/\text{kg)} \\ C_d = [2.2, 2.5, 2.8] \end{cases} \quad (10)$$

where  $S/M$  stands for the area-to-mass ratios. In a word, all elements of the training set are shown in Table 2.

The structure of the training set is illustrated in Figure 3, where  $t_0$  and  $t_{\text{end}}$  indicate the beginning and the end of the orbit epoch. Each sample consists of continuous data (time series vector of  $H$ ) and discrete data (other elements). Time series data is generated by HPOP with specific values of  $K_p$ ,  $F10.7$ ,  $i$ ,  $C_d$ ,  $S/M$ , and  $h_{t_0}$ . The sampling interval is set to 1 h.

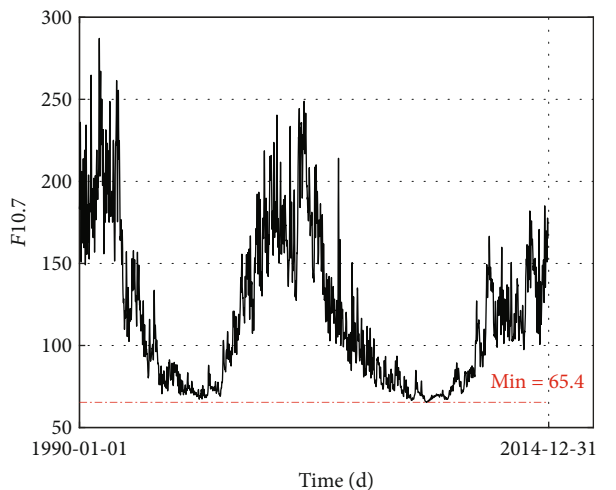


FIGURE 2: Daily observation of  $F10.7$ . Using the  $i$ -th data and the following 14 data points to calculate the  $i$ -th average observation value.

TABLE 2: The range of every element of training set.

Symbol	Element	Type	Range
$K_p$	Geomagnetic index	Discrete	[0, 27]
$F10.7$	Solar activity	Discrete	[70, 280]
$H$	Altitude (km)	Continuous	[150, 300]
$i$	Inclination (°)	Discrete	[90, 110]
$C_d$	Drag coefficient	Discrete	[2.2, 2.8]
$S/M$	Area-to-mass ratios ( $\text{m}^2/\text{kg}$ )	Discrete	[0.005, 0.02]

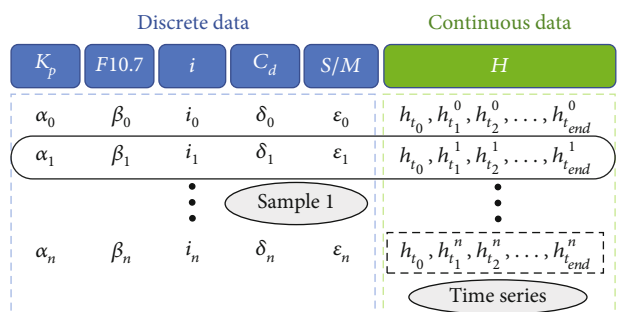


FIGURE 3: Structure of training set, whose initial altitude is fixed on  $h_{t_0}$ .

The values of  $K_p$ ,  $F10.7$ ,  $i$ ,  $C_d$ , and  $S/M$  are set as follows.

$$\begin{cases} K_p = \frac{n_1}{3} & (n_1 = 0, 1, 2 \dots, 27) \\ F10.7 = 70 + 5n_2 & (n_2 = 0, 1, 2 \dots, 42) \\ i = 90 + 10n_3 & (n_3 = 0, 1, 2) \\ C_d = 2.2 + 0.3n_4 & (n_4 = 0, 1, 2) \\ S/M = 0.005n_5 & (n_5 = 1, 2, 3, 4) \\ h_{t_0} = 210 + 20n_6 & (n_6 = 0, 1, 2, 3, 4) \end{cases} \quad (11)$$

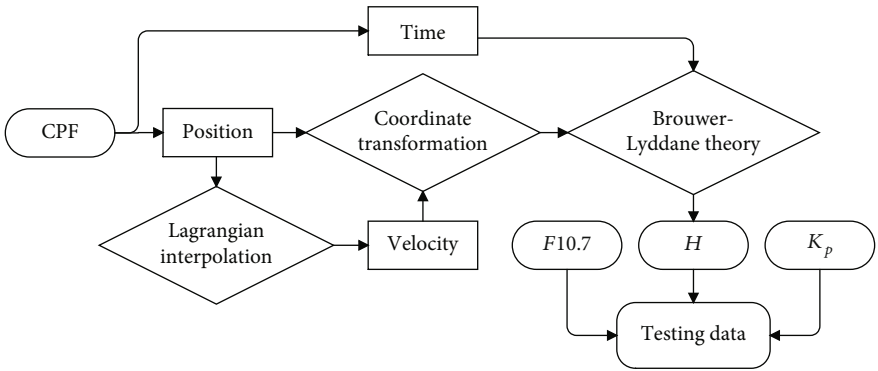
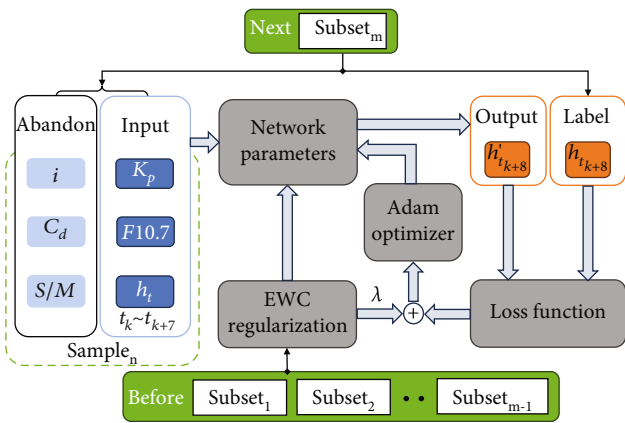
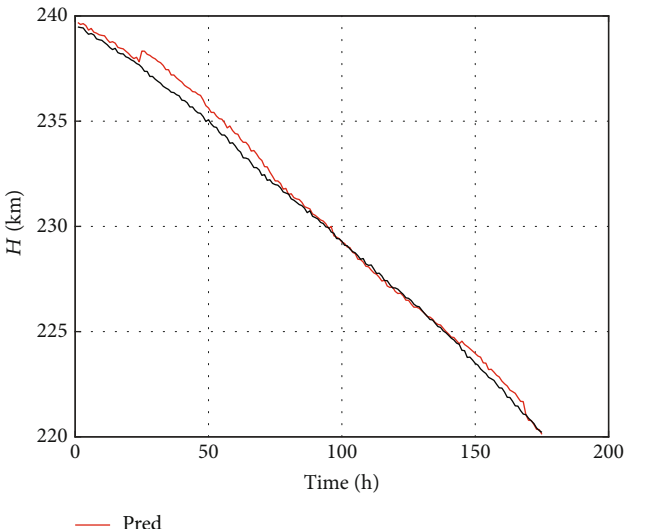
FIGURE 4: Process of converting CPF to the mean orbit elements of  $a$ .FIGURE 5: The  $m$ -th training of EODP.

TABLE 3: The architecture of NN.

Name	Description	Definition
Optimizer	Learning algorithm	Adam
Neurons of hidden layer	Layer 1 Layer 2 Layer 3 Layer 4	6 16 16 6
Activation function	Between Layer 1 and Layer 2 Between Layer 2 and Layer 3 Between Layer 3 and Layer 4	ReLU ReLU ReLU
Learning rate	—	0.005

A total of 216,720 samples are generated. With different values of  $K_p$ ,  $F10.7$ ,  $i$ ,  $C_d$ ,  $S/M$ , and  $h_{t_0}$ , the length of the time series in each sample may be different.

**2.2. Description of Orbital Decay Testing Set.** The testing set is crucial for evaluating MLT performance. In this study, VLEO spacecraft with precise location and no maneuvering

FIGURE 6: The decay prediction at the altitude of 240–220 km. Training the NN with the training subset of  $h_{t_0} = 220$ .

effects is the ideal test object. The model should fit well to the testing data produced by HPOP. Additionally, more realistic orbital data should be utilized. Data involved in the testing set consists of the following two parts:

- The CPF ephemeris files from the International Laser Ranging Service (ILRS).
- The data generated by HPOP.

CPF ephemeris is a high-precision forecast data derived from the advancement of satellite laser ranging technology [37]. CPF files are available from Crustal Dynamics Data Information System (CDDIS) or EUROLAS Data Center (EDC). CPF data is more precise during short-term forecasting than TLE and more credible due to continuous tracking and monitoring. The CPF data has a prediction error of less than 1 m for LEO spherical satellites and approximately 100 m for LEO nonspherical satellites, which can serve as a reference for the actual position of VLEO spacecraft. ILRS collects a portion of resident space object observation data,

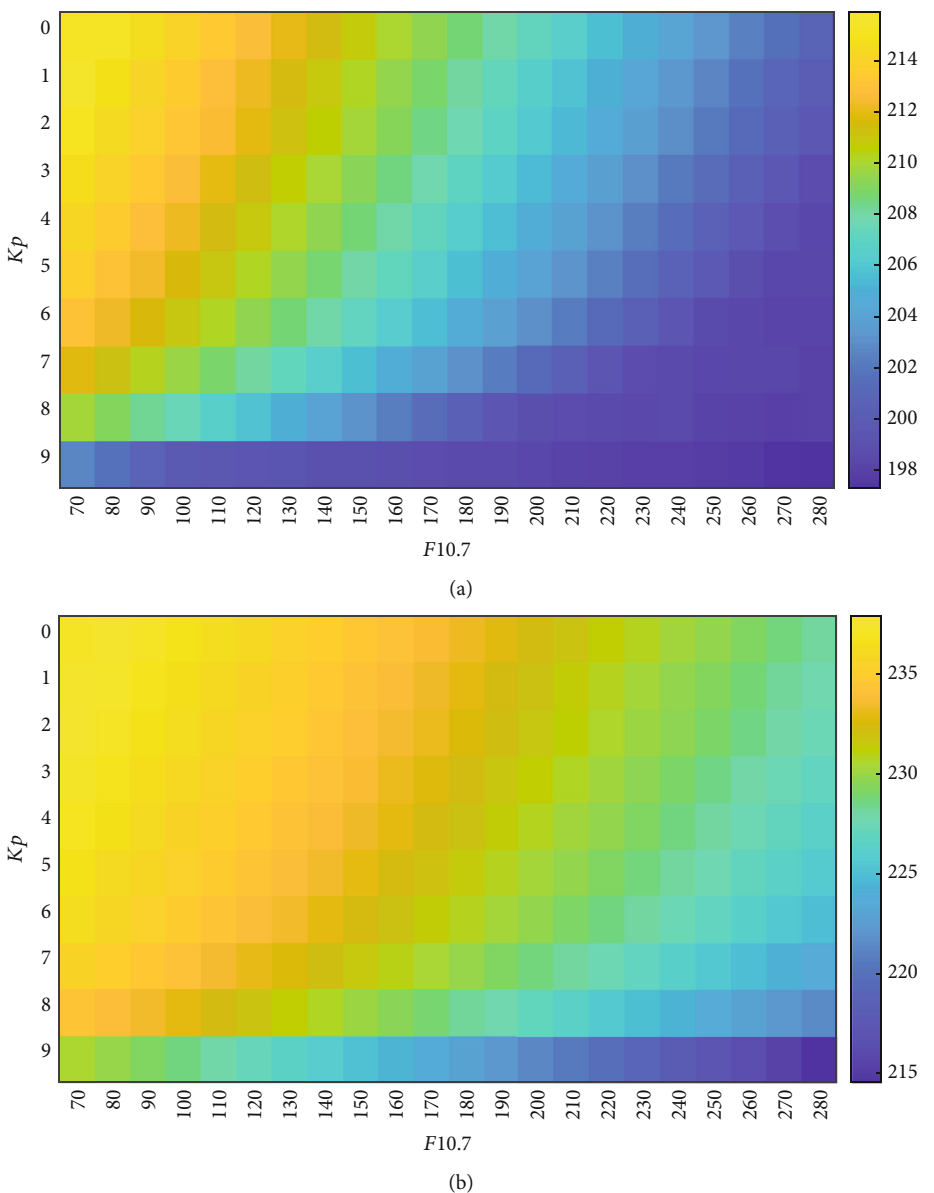


FIGURE 7: Continued.

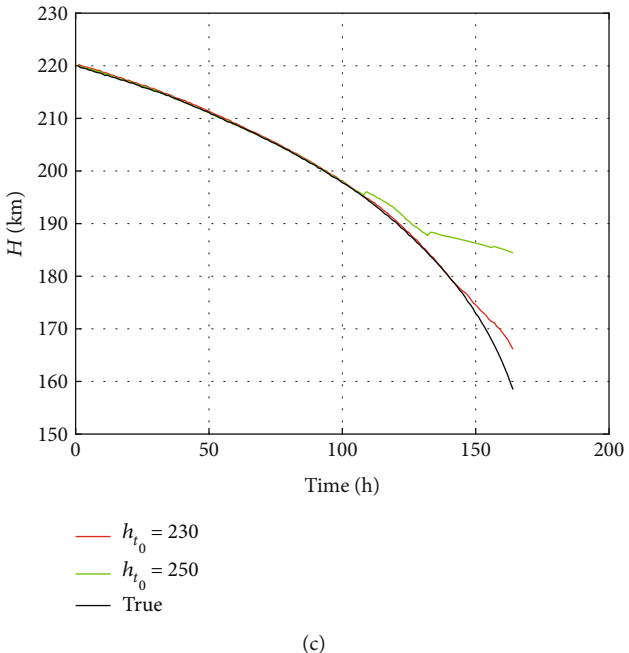


FIGURE 7: The effect of second elastic characteristic. (a) With  $K_p$  and  $F10.7$  vary within their range, the heatmap of the median of every time series data when  $h_{t_0} = 230$ . (b) With  $K_p$  and  $F10.7$  vary within their range, the heatmap of the median of every time series data when  $h_{t_0} = 250$ . (c) The prediction on the test data when model trained with subset<sub>1</sub> and subset<sub>2</sub>, respectively.

TABLE 4: Different training strategies.

Strategies	Set 1	Set 2	Set 3	Set 4
$h_{t_0}$ (km)	[210, 230, 250, 270, 290]	[210, 250, 290]	[230, 290]	[290, 230]

and the corresponding CPF data are provided by 29 institutes.

The CPF data contains information about the orbital epoch, sampling time, and position data in the earth-fixed coordinate system. With the process shown in Figure 4, the CPF data can be converted to testing set, mainly including  $H$ ,  $K_p$ , and  $F10.7$ , at the corresponding time. Orbital epoch, sampling time, and corresponding position data in CPF are first extracted and processed according to a standard format. Then, the 10th-order Lagrangian interpolation is applied to estimate the velocity information. With the Brouwer-Lyddane theory [38], which also can be described as Equation (2), processed data can be converted to  $H$ . The corresponding  $K_p$  and  $F10.7$  are obtained from CelestTrak.

**2.3. Description of EODP.** The proposed method, EODP, is an extensible application of DNN on PODP based on EWC, which is utilized to address the issue of catastrophic forgetting in MLT. The theory of EWC posits that knowledge or rules acquired during training are stored in the parameters (weights and bias) of NN. The primary approach of EWC to maintain memory in a dynamic environment involves the identification of critical parameters and the

implementation of a penalty function to constrain their significant alteration during subsequent training.

$H$  is the main object of concern, serving as both input and output. The orbit epoch of each sample is the primary factor influencing the extent of data redundancy. A sufficiently long-period epoch will bring a large amount of redundant data and easily lead to overfitting. In this study, training set is divided into several subsets based on the initial altitude, such as  $h_{t_0} = 230$  km or  $h_{t_0} = 250$  km, and the orbit epoch of each sample is limited to 3 days. Different training subsets stand for different rules of decay.

Training a model with all parameters obviously increases the computational complexity and the possibility of overfitting. The  $i$ ,  $C_d$ , and  $S/M$  do not serve as the key factors influencing the training of NN, which are not considered as the inputs. When training with Sample <sub>$n$</sub>  at time  $t_k$ , a time series consisting of  $K_p$ ,  $F10.7$ , and  $h_t$  in  $[t_k, t_{k+\Delta k}]$  is required as input. The time series will be labeled as  $h_{t_k+\Delta k+1}$ . In this study,  $\Delta k$  is set to 7. The input of historical observations (a time series) enables EODP to predict the future situation of decay accurately. From another perspective, historical observations implicitly contain the information of  $i$ ,  $C_d$ , and  $S/M$ , which can help avoid the challenge in determining

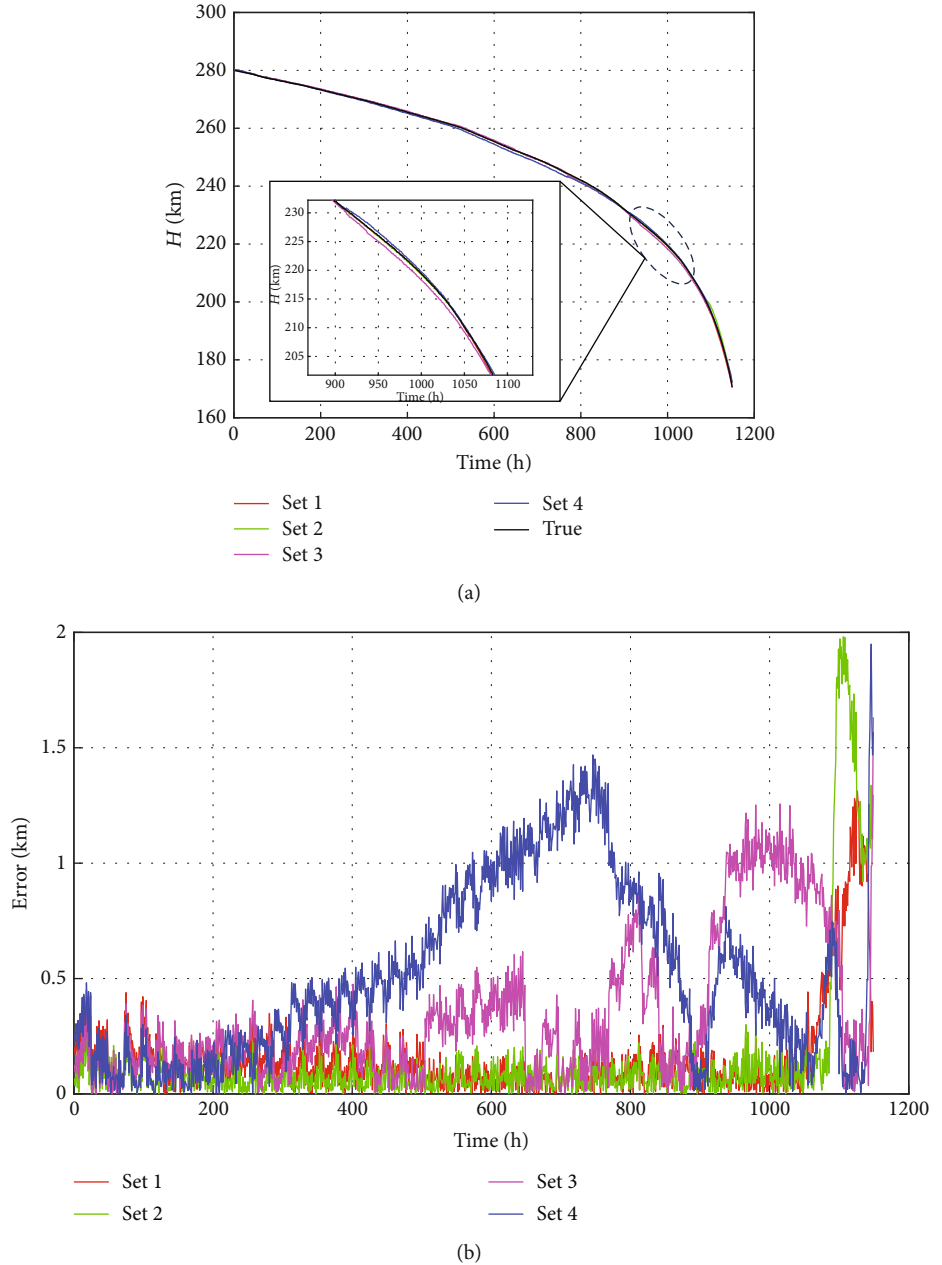


FIGURE 8: The performance of EODP trained with different strategies. (a) The performance of EODP relative to testing data. (b) Absolute errors of prediction relative to testing data.

TABLE 5: Evaluation of the performance of EODP trained with different strategies.

Strategies	RMSE (km)	Mean absolute error (km)	Median absolute error (km)
Set 1	0.2644	0.1677	0.1143
Set 2	0.3865	0.1678	0.0720
Set 3	0.7158	0.3999	0.2499
Set 4	0.8417	0.5564	0.4385

the physical parameters of specific spacecraft and correct errors introduced by the atmospheric model to some extent.

Figure 5 illustrates the process of the  $m$ -th training with Sample <sub>$n$</sub> . To capture the rule of Subset <sub>$m$</sub> , EWC regularization needs to be computed using the previous  $m - 1$  subsets.

The computation of  $m$ -th EWC regularization ( $L_m$ ) is related to the network parameters of last training, which can be described as

$$L_m = F_m \cdot \lambda_m \left( \theta_{\text{now}} - \theta'_{\text{before}} \right)^2 \quad (12)$$

TABLE 6: The initial state of real VLEO spacecraft.

Name	Number	Epoch	$i$ (°)	$h_{t_0}$ (km)	$C_d$	S/M ( $\text{m}^2/\text{kg}$ )
CHAMP	1	2010-08-04 00:00:00	51.61	263.8	2.91	0.00497
		2010-08-08 24:00:00				
	2	2010-08-24 00:00:00	51.61	255.0	2.91	0.00497
		2010-08-28 24:00:00				
ANDE Pollux	1	2010-03-08 00:00:00	87.18	269.3	2.116	0.007316
		2010-03-13 24:00:00				
	2	2010-08-20 00:00:00	87.18	243.4	2.116	0.007316
		2010-08-25 24:00:00				

where the matrix  $\theta_{\text{now}}$  and  $\theta'_{\text{before}}$  indicate current and previous network parameters (weights and bias), respectively,  $\lambda_m$  stands for the  $m$ -th significant coefficient of learned knowledge from  $m - 1$  subsets, and  $F_m$  represents the  $m$ -th weight matrix of all network parameters, which is a diagonal matrix. Elements of  $F_m$  come from the average gradient variation of network parameters, which are described as follows:

$$f_{nn} = \frac{1}{N} \sum_{a_j \in A} \text{grad}\left(\theta'_n | a_j\right)^2 \quad (13)$$

where  $f_{nn}$  is the  $n$ -th diagonal element of  $F_m$ ,  $A$  represents the previously used training subsets,  $N$  is the number of samples in Subset <sub>$m$</sub> ,  $\theta'_n$  is the  $n$ -th network parameter of  $\theta'_{\text{before}}$ , and  $a_j$  is the  $j$ -th sample of  $A$ .

### 3. Feature Analysis of EODP

**3.1. Plasticity of Network Parameters.** EODP extends the ability to master the rules from different training subsets by modulating the plasticity of network parameters. The plasticity of network parameters is a fundamental feature of NN, which is manifested in two perspectives. (1) The NN trained with the current subset can be applied in other scenarios. (2) NN exhibits varying performance in different regions due to differing densities of the same training subset. The architecture of NN is shown in Table 3.

The model trained with the subset of  $h_{t_0} = 220$  is also applicable to the altitude of 240–220 km, illustrating the first aspect of plasticity, as depicted in Figure 6.

As the heatmaps shown in Figures 7(a) and 7(b), the data distribution in the training subset<sub>1</sub> ( $h_{t_0} = 230$ ) and subset<sub>2</sub> ( $h_{t_0} = 250$ ) is different. Data in subset<sub>1</sub> is more concentrated at altitudes of less than 200 km, while data in subset<sub>2</sub> is completely opposite. The performance of NN trained with subset<sub>1</sub> is better than that trained with subset<sub>2</sub> at the altitudes around 200 km, which reflects the second perspective.

**3.2. Application of Plasticity in Training Strategies.** Plasticity plays a crucial role in the training strategies of EODP, involving the utilization of different combinations of training subsets. With a reasonable size of training set, the achievement of exceptional performance is enabled. When

analyzing the decay at altitudes ranging from 150 to 300 km, various combinations of training subsets are outlined in Table 4. Testing data is generated by HPOP, with an initial altitude of 280 km and an orbit epoch of around 50 days.

EODP is subjected to various training strategies as outlined in Table 4, and its performance is illustrated in Figure 8. EODP, when trained with each dataset, consistently demonstrates exceptional performance throughout the entire orbit epoch of the test data. The analysis of absolute errors in Figure 8(b) reveals that EODP, when trained with extensive data (such as Set 1 and Set 2), exhibits more stable and accurate performance. Towards the end of the orbit epoch, there is a notable spike in errors, which is attributed to the limited time interval for sample generation. The narrow epoch interval results in sparse data at lower altitudes, leading to a marginal decline in prediction accuracy. This scenario is particularly pronounced in models trained with Set 3 and Set 4.

The performance depicted in Figure 8 is assessed using statistical metrics, including root mean squared error (RMSE, primarily considered), median absolute error, and mean absolute error. As illustrated in Table 5, the performance of the EODP trained with Set 1 and Set 2 surpasses that of Set 3 and Set 4, suggesting that a more extensive training data leads to enhanced overall prediction accuracy. In certain instances, obtaining  $\lambda$  becomes challenging with a large number of training subsets, which will easily result in heightened prediction volatility. The training approach becomes more adaptable due to the plasticity effect. In comparison to Set 1, the performance of the model trained with Set 2 is considered satisfactory in certain instances, indicating the potential for regulating the size of the training set.

### 4. Results on Real Case

The performance of EODP, trained with Set 1, is analyzed in real-world scenarios. To avoid the negative effects of maneuvers, spacecraft at the end of their lifetime are suitable as test objects, such as CHAMP and ANDE Pollux. Table 6 illustrates the initial states of the two spacecraft at specific orbit epochs. The  $h_{t_0}$  can be inverted from CPF data.  $C_d$  and S/M are estimated from official technical documents [7]. Testing data from HPOP is generated based on the same

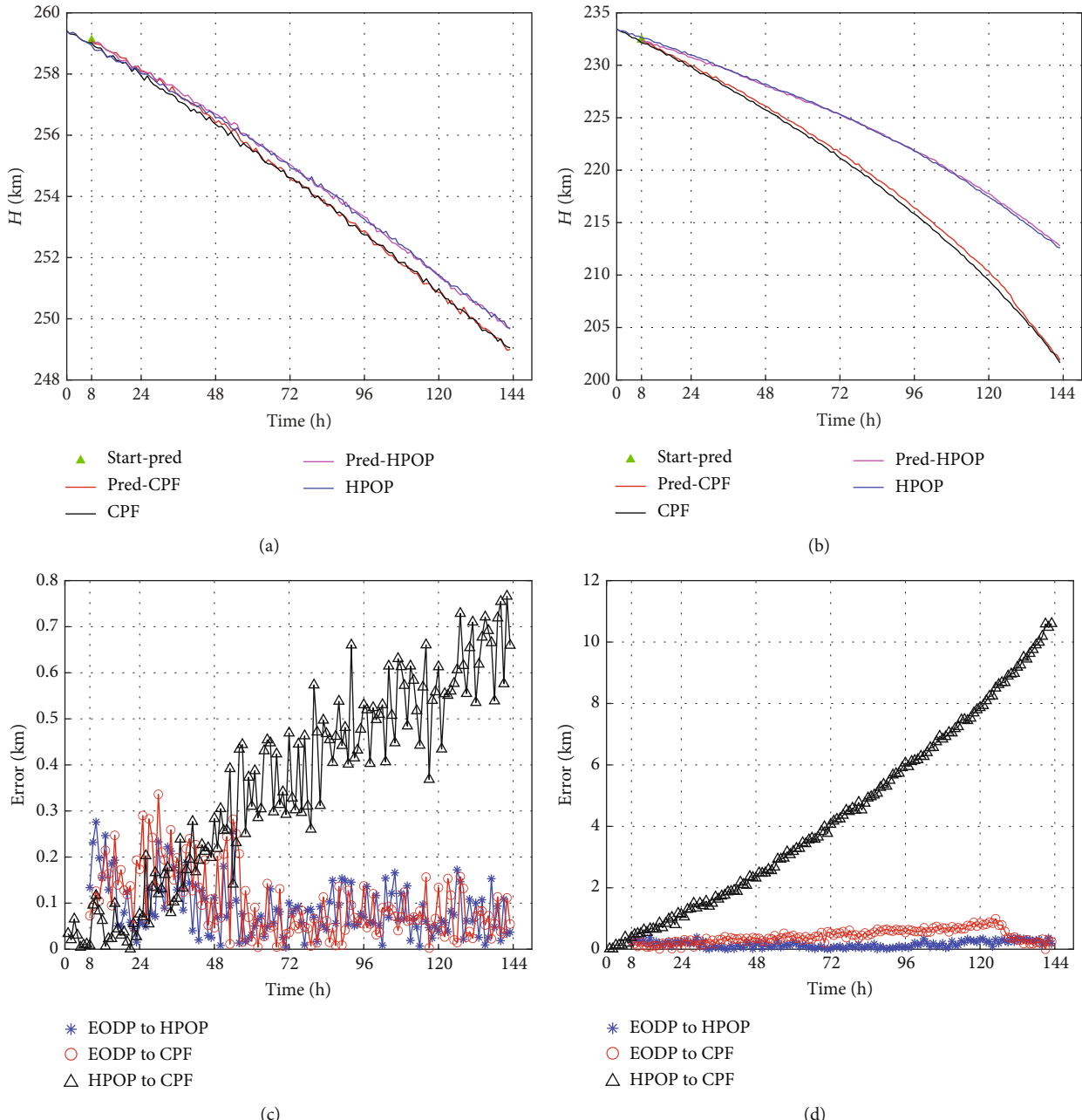


FIGURE 9: Decay prediction of ANDE Pollux with EODP and the corresponding errors. (a) Decay prediction of ANDE Pollux in the first orbit epoch. The first value of predicting occurs at Hour 8. (b) Decay prediction of ANDE Pollux in the second orbit epoch. The first value of predicting occurs at Hour 8. (c) The absolute errors of prediction with EODP relative to testing data (HPOP and CPF) and the accuracy of HPOP data in comparison to CPF data in the first orbit epoch of ANDE Pollux. (d) The absolute errors of prediction with EODP relative to testing data (HPOP and CPF) and the accuracy of HPOP data in comparison to CPF data in the second orbit epoch of ANDE Pollux.

state.  $F10.7$  and  $K_p$  are derived from the observational data, which is sampled once a day.

The performance on actual cases of CHAMP and ANDE Pollux with the EODP is illustrated in Figures 9 and 10. The EODP shows outstanding performance on testing data created by HPOP, with a maximum absolute error of around 0.3 km. With a maximum absolute error of less than 1 km in 136 h, EODP also achieves PODP on real VLEO spacecraft.

When analyzing the same spacecraft, the performance of EODP varies at different altitudes. The increasing prediction error in some cases is caused by data sparsity at low altitudes and inappropriate values of  $\lambda$  that leads to a marginal decline in prediction accuracy. Different values of  $\lambda$  for distinct training subsets indicate varying levels of focus on these rules, leading to different performance in various situations.

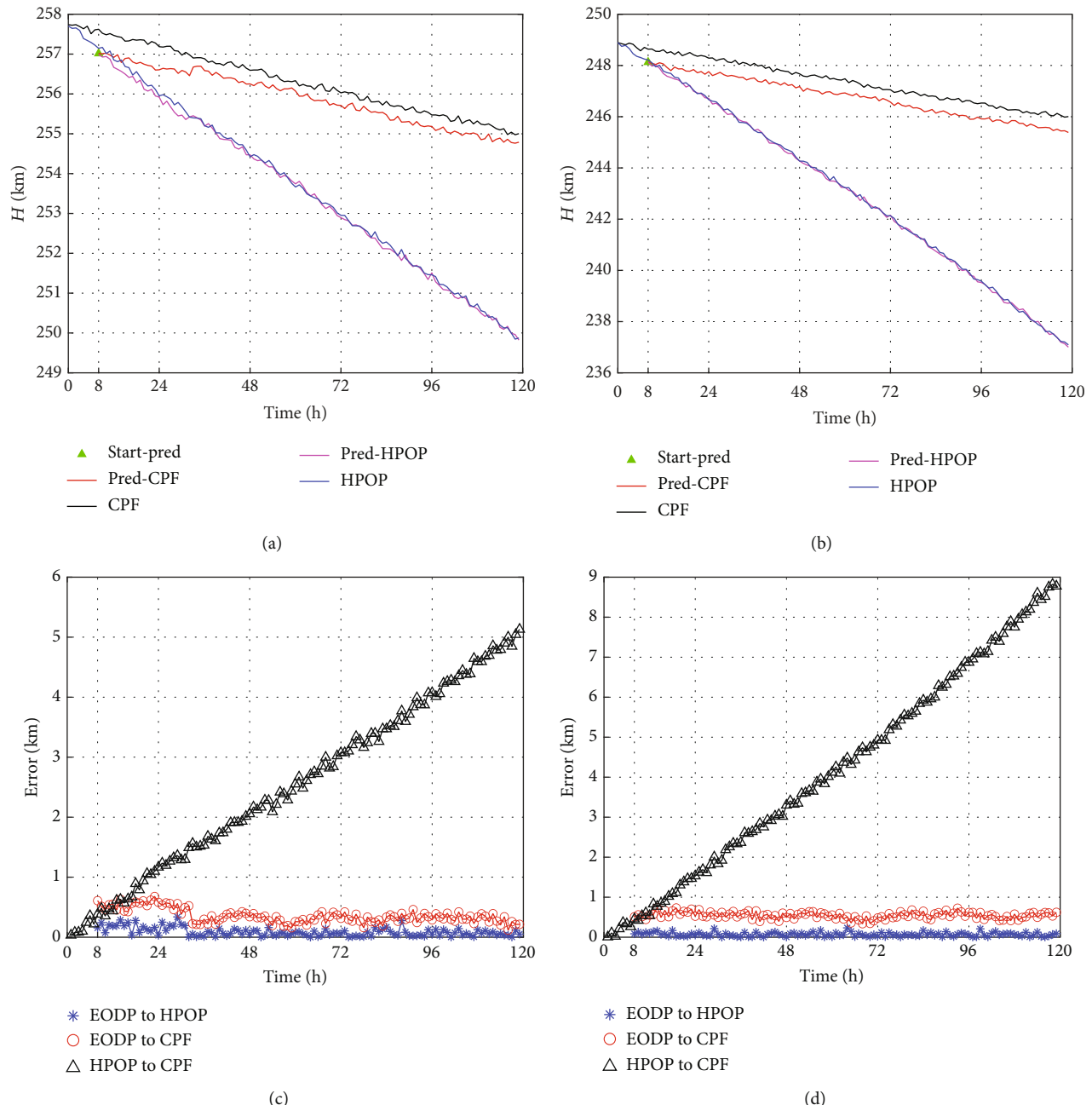


FIGURE 10: Decay prediction of CHAMP with EODP and the corresponding errors. (a) Decay prediction of CHAMP in the first orbit epoch. The first value of predicting occurs at Hour 8. (b) Decay prediction of CHAMP in the second orbit epoch. The first value of predicting occurs at Hour 8. (c) The absolute errors of prediction with EODP relative to testing data (HPOP and CPF) and the accuracy of HPOP data in comparison to CPF data in the first orbit epoch of CHAMP. (d) The absolute errors of prediction relative to testing data (HPOP and CPF) and accuracy of HPOP data in comparison to CPF data in the second orbit epoch of CHAMP.

A significant disparity between HPOP data and CPF data is mainly due to the inherent limitations of TOPM, uncertainties in physical parameters, and future space environment, leading to deteriorating performance. For specific spacecraft with a spherical shell and stable surface materials (such as ANDE Pollux), TOPM can perform well in PODP. In fact, the  $C_d$  and  $S/M$  of the CHAMP vary during decaying, which leads to critical error prediction. Due to the lack

of equivalent accuracy in the parameters, the error of the testing data generated by HPOP relative to CPF is quite different. In this study, the proposed method, EODP, effectively overcomes the challenge of estimating physical parameters and achieves higher accuracy in PODP.

RMSE, median error, and mean error are used to evaluate the performance of EODP on actual cases, as shown in Tables 7, 8, and 9. EODP can be applied to various scenarios.

TABLE 7: The RMSE of the prediction and the improvement of EODP compared to HPOP.

RMSE	Epoch	EODP-HPOP (km)	EODP-CPF (km)	HPOP-CPF (km)	Improvement
ANDE Pollux	1	0.1063	0.1241	0.4187	70.36%
	2	0.1907	0.4781	5.4531	91.23%
CHAMP	1	0.1146	0.3765	2.9730	87.34%
	2	0.0854	0.5538	4.9998	88.92%

TABLE 8: The median absolute error of the prediction and the improvement of EODP compared to HPOP.

Median absolute error	Epoch	EODP-HPOP (km)	EODP-CPF (km)	HPOP-CPF (km)	Improvement
ANDE Pollux	1	0.0734	0.0824	0.4016	79.48%
	2	0.1413	0.3850	4.1691	90.77%
CHAMP	1	0.0684	0.3382	2.5514	86.74%
	2	0.0619	0.5521	4.1210	86.60%

TABLE 9: The mean absolute error of the prediction and the improvement of EODP compared to HPOP.

Mean absolute error	Epoch	EODP-HPOP (km)	EODP-CPF (km)	HPOP-CPF (km)	Improvement
ANDE Pollux	1	0.0886	0.1006	0.3584	71.93%
	2	0.1592	0.4263	4.4959	90.52%
CHAMP	1	0.0884	0.3567	2.5883	86.22%
	2	0.0693	0.5474	4.2640	87.16%

Compared to HPOP for lower altitude cases, the accuracy is enhanced by approximately 90%, such as the second orbit epoch of ANDE Pollux (5 days) and CHAMP (6 days). For higher altitudes, the prediction accuracy is improved by at least 70%.

## 5. Conclusion

In this paper, the proposed method of EODP for implementing PODP based on historical data demonstrates high accuracy. EODP leverages the EWC, a method of continual learning, and addresses the limited generalization ability. This results in improved performance on PODP for various spacecraft and enhances the applicability of MLT in orbit prediction. EODP also overcomes the challenge of inaccurate physical parameter and future space environment estimation. Meanwhile, the EODP can be further extended by adjusting the initial altitude and important coefficients of different training subsets. This implies that the EODP can be utilized for PODP covering all LEO and VLEO spacecraft, including space debris. With EODP, powerful data support is easily provided for orbit maintenance and high-precision flight control of spacecraft.

## Data Availability Statement

The data that support the findings of this study are available from the corresponding author upon reasonable request.

## Conflicts of Interest

The authors declare no conflicts of interest.

## Funding

This research is supported by the National Science Fund for Distinguished Young Scholars (doi: 10.13039/501100014219) (12125207) and National Natural Science Foundation of China (doi: 10.13039/501100001809) (12372052). The authors are grateful for the financial support from Technology Innovation Team of Manned Space Engineering.

## Acknowledgments

This work is supported by the National Science Fund for Distinguished Young Scholars (No. 12125207) and the National Natural Science Foundation of China (No. 12372052). The authors are grateful for the financial support from Technology Innovation Team of Manned Space Engineering.

## References

- [1] J. Virgili-Llop, P. Roberts, D. Z. Hao, L. Ramio-Tomas, and V. Beauplet, “Very low earth orbit mission concepts for earth observation: benefits and challenges,” in *Reinventing space conference*, Springer, 2014.
- [2] N. H. Crisp, P. C. E. Roberts, S. Livadiotti et al., “The benefits of very low earth orbit for earth observation missions,” *Progress in Aerospace Sciences*, vol. 117, article 100619, 2020.

- [3] N. Hayashi, A. Weiss, and S. Di Cairano, "Model predictive control approach for autonomous sun-synchronous sub-recurrent orbit control," in *AIAA Scitech 2021 Forum*, American Institute of Aeronautics and Astronautics, 2021.
- [4] P. Williams and I. Faruque, "Orbital debris encounter estimation for international space station orbit companion satellites," in *ASCEND 2023*, American Institute of Aeronautics and Astronautics, 2023.
- [5] C. Pardini and L. Anselmo, "Monitoring the orbital decay of the Chinese space station Tiangong-1 from the loss of control until the re-entry into the earth's atmosphere," *Journal of Space Safety Engineering*, vol. 6, no. 4, pp. 265–275, 2019.
- [6] R. Haagmans, D. Muzi, A. Popescu, R. Floberghagen, M. Kern, and M. Fehringer, "The GOCE Gravity Mission: ESA's First Core Explorer," *3rd GOCE User Workshop*, vol. 68, 2007.
- [7] A. C. Nicholas, G. C. Gilbreath, S. E. Thonnard, R. A. Kessel, R. Lucke, and C. P. Sillman, "The Atmospheric Neutral Density Experiment (ANDE) and Modulating Retroreflector in Space (MODRAS): combined flight experiments for the space test program," in *International Symposium on Remote Sensing*, Crete, Greece, 2003.
- [8] H. Kawasaki, K. Konoue, H. Hoshino, Y. Kaneko, and M. Sasaki, "Interim report of super low altitude satellite operation," in *IGARSS 2018 - 2018 IEEE International Geoscience and Remote Sensing Symposium*, Valencia, Spain, 2018.
- [9] J. Wilson, J. Nealy, G. de Angelis, F. Badavi, F. Cucinotta, and M. Kim, "Dynamic/anisotropic low earth orbit environmental models," in *AIAA space 2003 conference & exposition*, Long Beach, California, 2003.
- [10] X. Gao, Z. Li, Q. Chen, D. Ding, and A. Peng, "Prediction of orbit decay for large-scale spacecraft considering rarefied aerodynamic perturbation effects," *International Journal of Aerospace Engineering*, vol. 2022, Article ID e8984056, 13 pages, 2022.
- [11] N. Cimmino, R. Opronolla, and G. Fasano, "Machine learning-based approach for ballistic coefficient estimation of resident space objects in LEO," *Advances in Space Research*, vol. 71, no. 12, pp. 5007–5025, 2023.
- [12] Q. Lei and H. Zhang, "Orbit prediction method for space station based on PPO2 algorithm of reinforcement learning," *China Space Science and Technology*, vol. 43, no. 4, pp. 93–103, 2023.
- [13] H. Peng and X. Bai, "Artificial neural network-based machine learning approach to improve orbit prediction accuracy," *Journal of Spacecraft and Rockets*, vol. 55, no. 5, pp. 1248–1260, 2018.
- [14] B. Li, J. Huang, Y. Feng, F. Wang, and J. Sang, "A machine learning-based approach for improved orbit predictions of LEO space debris with sparse tracking data from a single station," *IEEE Transactions on Aerospace and Electronic Systems*, vol. 56, no. 6, pp. 4253–4268, 2020.
- [15] H. Bzialion, A. Guillot, A. Petit, and R. Lucken, "Systematic TLE data improvement by neural network for most cataloged resident space objects," *Advances in Space Research*, vol. 72, no. 7, pp. 2649–2659, 2023.
- [16] M. Thammawichai and T. Luangwilai, "Data-driven satellite orbit prediction using two-line elements," *Astronomy and Computing*, vol. 46, article 100782, 2024.
- [17] F. Luo, H. Ren, and B. Zhao, "Research on satellite orbit forecast based on neural network algorithm," *Ship Science and Technology*, vol. 42, no. 19, pp. 146–151, 2020.
- [18] A. Kutalev, "Natural way to overcome the catastrophic forgetting in neural networks," 2020, <https://arxiv.org/abs/2005.07107>.
- [19] L. Wang, X. Zhang, H. Su, and J. Zhu, "A comprehensive survey of continual learning: theory, method and application," *IEEE Transactions on Pattern Analysis and Machine Intelligence*, vol. 46, no. 8, 2024.
- [20] C. Finn, P. Abbeel, and S. Levine, "Model-agnostic meta-learning for fast adaptation of deep networks," *International conference on machine learning*, 2017, pp. 1126–1135, PMLR, 2017.
- [21] T. Schaul, J. Quan, I. Antonoglou, and D. Silver, "Prioritized experience replay," 2015, <https://arxiv.org/abs/1511.05952>.
- [22] J. Irkpatrick, R. Pascanu, N. Rabinowitz et al., "Overcoming catastrophic forgetting in neural networks," *Proceedings of the National Academy of Sciences*, vol. 114, no. 13, pp. 3521–3526, 2017.
- [23] A. Scorsoglio, A. D'Ambrosio, L. Ghilardi, B. Gaudet, F. Curti, and R. Furfaro, "Image-based deep reinforcement meta-learning for autonomous lunar landing," *Journal of Spacecraft and Rockets*, vol. 59, no. 1, pp. 153–165, 2022.
- [24] A. Scorsoglio, A. D'Ambrosio, L. Ghilardi et al., "Safe lunar landing via images: a reinforcement meta-learning application to autonomous hazard avoidance and landing," in *In Proceedings of the 2020 AAS/AIAA Astrodynamics Specialist Conference*, pp. 9–12, Lake Tahoe Resort Hotel in South Lake Tahoe, CA, 2020, Virtual.
- [25] L. Federici, A. Scorsoglio, L. Ghilardi et al., "Image-based meta-reinforcement learning for autonomous guidance of an asteroid impactor," *Journal of Guidance, Control, and Dynamics*, vol. 45, no. 11, pp. 2013–2028, 2022.
- [26] J. Wu, C. Wei, H. Zhang, Y. Liu, M. Zhang, and H. Wang, "Learning-based spacecraft reactive anti-hostile-rendezvous maneuver control in complex space environments," *Advances in Space Research*, vol. 72, no. 10, pp. 4531–4552, 2023.
- [27] Z. Wen, L. Li, J. Song, S. Zhang, and H. Hu, "Scheduling single-satellite observation and transmission tasks by using hybrid actor-critic reinforcement learning," *Advances in Space Research*, vol. 71, no. 9, pp. 3883–3896, 2023.
- [28] V. Marsocci and S. Scardapane, "Continual Barlow twins: continual self-supervised learning for remote sensing semantic segmentation," *IEEE Journal of Selected Topics in Applied Earth Observations and Remote Sensing*, vol. 16, pp. 5049–5060, 2023.
- [29] D. Brouwer, "Solution of the problem of artificial satellite theory without drag," *The Astronomical Journal*, vol. 64, p. 378, 1959.
- [30] A. C. Long, J. O. Cappellari, C. E. Velez, and A. J. Fuchs, *Goddard trajectory determination system (GTDS) mathematical theory*, NASA Goddard Space Flight Center, 1989.
- [31] J. Virgili Llop, P. C. E. Roberts, K. Palmer, S. Hobbs, and J. Kingston, "Descending sun-synchronous orbits with aerodynamic inclination correction," *Journal of Guidance, Control, and Dynamics*, vol. 38, no. 5, pp. 831–842, 2015.
- [32] T. Liang, K. Nie, Q. Li, and J. Zhang, "Advanced analytical model for orbital aerodynamic prediction in LEO," *Advances in Space Research*, vol. 71, no. 1, pp. 507–524, 2023.
- [33] B. Bowman, W. K. Tobiska, F. Marcos, C. Huang, C. Lin, and W. Burke, "A new empirical thermospheric density model JB2008 using new solar and geomagnetic indices," in *AIAA/AAS astrodynamics specialist conference and exhibit*, pp. 2008–6348, Honolulu, Hawaii, 2008.

- [34] V. U. J. Nwankwo and S. K. Chakrabarti, "Effects of space weather on the ionosphere and LEO satellites' orbital trajectory in equatorial, low and middle latitude," *Advances in Space Research*, vol. 61, no. 7, pp. 1880–1889, 2018.
- [35] L. McCreary, "A satellite mission concept for high drag environments," *Aerospace Science and Technology*, vol. 92, pp. 972–989, 2019.
- [36] J. Matzka, C. Stolle, Y. Yamazaki, O. Bronkalla, and A. Morschhauser, "The Geomagnetic  $K_p$  index and derived indices of geomagnetic activity," *Space Weather*, vol. 19, no. 5, article e2020SW002641, 2021.
- [37] M. R. Pearlman, J. J. Degnan, and J. M. Bosworth, "The International Laser Ranging Service," *Advances in Space Research*, vol. 30, no. 2, pp. 135–143, 2002.
- [38] R. H. Lyddane, "Small eccentricities or inclinations in the Brouwer theory of the artificial satellite," *The Astronomical Journal*, vol. 68, p. 555, 1963.